An Experimental Study of Steam-Solvent Coinjection for Bitumen Recovery Using a Large-Scale Physical Model

Kai Sheng and **Ryosuke Okuno,** University of Texas at Austin;
Abdullah Al-Gawfi, Petro Nakutnyy, and **Muhammad Imran,** Saskatchewan Research Council; and
Kazunori Nakagawa, Japan Canada Oil Sands Ltd

Summary

In this paper, we present a solvent-assisted steam-assisted gravity drainage (SA-SAGD) experiment with multicomponent solvent (i.e., condensate) using a large physical model. The sandpack for the experiment had a porosity of 0.33 and a permeability of 5.6 darcies in the cylindrical pressure vessel that was 1.22 m in length and 0.425 m in internal diameter. The sandpack was initially saturated with 93% Athabasca bitumen and 7% deionized water. The main objective of this research was to study the in-situ thermal/compositional flow and produced bitumen properties in SA-SAGD with condensate.

After the preheating of the sandpack for 24 hours, SA-SAGD with 2.8-mol% condensate was performed at 50 cm^3/min (cold-water equivalent) at 3500 kPa for 3 days. The experimental data of production, injection, and temperature distribution were recorded. Also, 10 samples of produced oil were taken and analyzed for density and asphaltene content. The sandpack was excavated after the experiment to analyze the asphaltene content in the remaining oil at different locations. A numerical simulation model was calibrated based on the data of material balance and temperature distribution, and it was validated with properties of the produced and excavated samples. The simulation model used fluid models based on experimental data of viscosities, densities, and bubblepoints for four condensate/bitumen mixtures.

Results showed that SA-SAGD was efficient in bitumen recovery with a cumulative steam-to-oil ratio (SOR) that was two to three times smaller than that in SAGD using the same physical model. Detailed analysis of the calibrated simulation model indicated that SA-SAGD enabled the steam chamber to expand more efficiently with a smaller amount of water throughput than SAGD. Volatile solvent components tended to remain in the chamber, and the condensed solvent components acted as a miscible carrier for bitumen components. The analysis further showed that the more efficient oil recovery in SA-SAGD occurred with predominantly cocurrent flow of oil and water near the chamber edge. SA-SAGD recovered a larger amount of asphaltene components (i.e., less in-situ upgrading) than SAGD likely because of its lower chamber temperature, shorter production period, and enhanced local displacement efficiency.

Introduction

SAGD is a commercially successful method for bitumen recovery. SAGD uses a pair of horizontal wells; one of them is to inject high-quality steam, and the other is to produce the mobilized bitumen that flows under gravity along the edge of a steam-saturated zone, a "steam chamber." SAGD requires a large amount of steam to mobilize in-situ bitumen for an economically feasible production rate.

SA-SAGD is a variant of SAGD that injects steam with a small amount of volatile hydrocarbon solvent to improve the energy efficiency of SAGD. The vaporization and condensation behavior of the solvent components has been studied as an important mechanism in SA-SAGD (Dong 2012; Hosseininejad Mohebati et al. 2012; Keshavarz et al. 2014, 2015; Venkatramani and Okuno 2017, 2018; Sheng et al. 2018; Ovalles 2019; Zirahi et al. 2020). The injected solvent propagates as part of the vapor phase and condenses near the edge of the steam chamber. The mobility of bitumen near the steam chamber is increased mainly by the latent heat released from the condensing vapor and the mixing with condensed solvent. The oil phase that flows under gravity contains the condensed solvent and bitumen components. The mass transfer across the chamber edge is expected to be significant for volatile components: condensation from inside to outside the steam chamber and vaporization in the opposite direction. This type of interphase mass transfer near thermal fronts ("distillation") has been known in steam injection (with no solvent injection) for conventional heavy oil, in which the reservoir oil contains a larger number of volatile components than bitumen. The distillation mechanism can yield an efficient oil displacement by leaving only a small fraction of bitumen behind the thermal fronts (Prats 1982).

One of the effective and widely available solvents for SA-SAGD is condensate, which is a mixture of hydrocarbons (Nasr et al. 2003). Coinjection of multicomponent solvent with steam has been experimentally studied in a limited number of publications (Deng et al. 2010; Ayodele et al. 2009; Khaledi et al. 2012, 2015; Jha et al. 2013; Al-Murayri et al. 2016a, 2016b; Mukhametshina et al. 2016). Khaledi et al. (2012) studied the energy efficiency of condensate-steam coinjection in comparison to SAGD in a large physical model by using two different condensate samples. Al-Murayri et al. (2016a, 2016b) tested naptha and condensates, which are both mixtures of hydrocarbons, in a 3D physical model. Those experiments have shown an improved energy efficiency in comparison to SAGD and an increased asphaltene content in the remaining oil.

Simulation studies have been published for condensate-steam coinjection. Khaledi et al. (2015) simulated three different condensates as multipseudocomponents in their simulation at low-pressure operation conditions for SA-SAGD. They found that the amount of noncondensable gas might affect the SA-SAGD performance. A few publications studied the distribution of condensate components in the reservoir during condensate-steam coinjection (Ivory et al. 2008; Deng et al. 2010).

Sheng et al. (2020b) performed a SAGD experiment in a large physical model. Their experimental results showed that the produced bitumen was lighter and contained up to 5-wt% less asphaltenes than the original bitumen, which was attributed to the distillation mechanism by volatile bitumen components. Their history-matched simulation indicated a transition in flow regime in their SAGD experiment. The mixed flow regimes were dominated by countercurrent flow of water and oil when a steam chamber started to expand. Then, cocurrent flow of water and oil became dominant when the steam chamber had developed in the experiment. The transition in flow

Original manuscript received for review 17 February 2021. Revised manuscript received for review 14 May 2021. Paper (SPE 205158) peer approved 18 May 2021.

regime was explained based on the studies by Bourbiaux and Kalaydjian (1990), Kalaydjian (1990), Bentsen and Manai (1993), Haugen et al. (2015), and Andersen et al. (2020). The capillary-induced water imbibition near the edge of a SAGD steam chamber can be particularly important for water-soluble solvents proposed for enhancing the efficiency of SAGD, such as dimethyl ether (Okuno 2018; Sheng et al. 2018; Baek et al. 2019b; Khalifi et al. 2020), organic alkalis (Baek et al. 2019a; Sheng et al. 2020a), and ethyl acetate (Zirahi et al. 2020) because it is conducive to an enhanced level of mixing between the injected solvent and bitumen.

In this paper, we present an experimental study of thermal/compositional flow in SA-SAGD with condensate by using a large physical model. The objective of this paper was to investigate the use of multicomponent solvent in SA-SAGD in terms of in-situ flow regimes, thermal/compositional flow, and produced fluid properties; this can be viewed as a comparative study with the SAGD experiment using the same experimental setup (Sheng et al. 2020b). The SA-SAGD experimental data, including material balance and temperature distributions, were history matched by using a numerical simulation model. The fluid models used in the simulation were based on phase behavior experimental data for bitumen/condensate mixtures.

In the following sections, the experimental methods are first described. Then, the experimental results and the history matching are presented and discussed. Finally, the main conclusions are presented.

SA-SAGD Experimental Setup and Operations

This section presents the 3D physical model apparatus, fluid properties, and procedures for packing and saturating the model. Then, the SA-SAGD experiment is described, including preheating, winddown, fluid sampling, and post-run model degassing and excavation. The experimental setup and sandpack design were based largely on the SAGD experiment by Sheng et al. (2020b); therefore, the subsequent "SAGD experiment" refers to their research.

Experimental Apparatus. Fig. 1 shows a schematic of the SA-SAGD experimental setup (Saskatchewan Research Council). The main components were a carbon-steel cylindrical pressure vessel, carbon-steel flanges designed for the insertion of two horizontal wells and a grid of thermocouples, and centralized inline heaters for the injection and production wells equipped with multipoint thermocouple strings on their surfaces. Apart from the cylindrical vessel, the experimental setup consisted of a steam generator; high-pressure injection pumps for water and solvent injection; automated production tanks; online gas chromatography for live gas compositional analysis; pressure gauges; a wet test meter to measure the volumes of the produced gases; and a data acquisition system to monitor, control, and record all operational parameters.

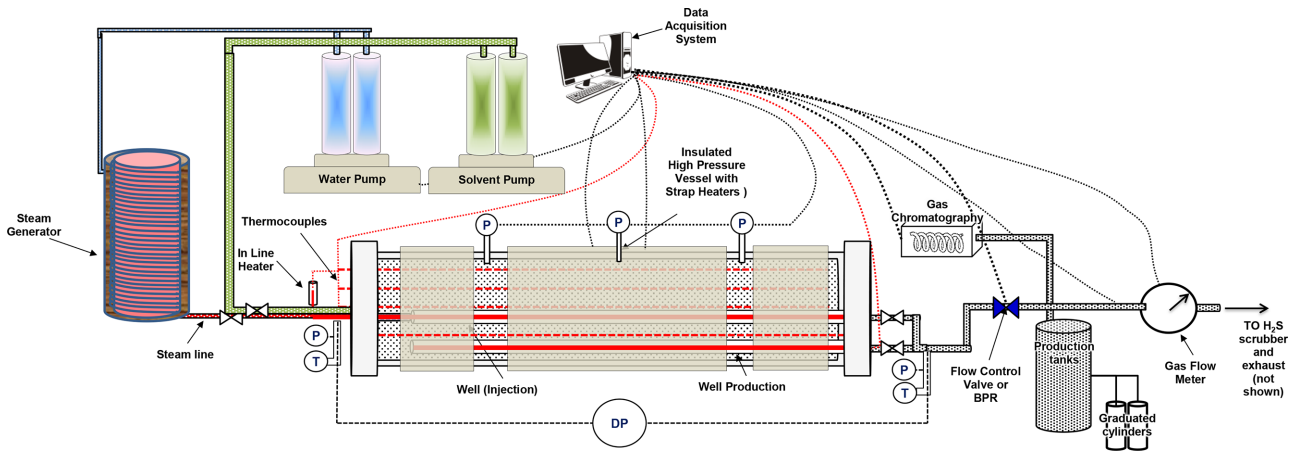

Fig. 1—Schematic of the SA-SAGD experimental setup. BPR, DP, P, and T in the figure are backpressure regulator, pressure transducer for pressure drop measurements, pressure gauge, and temperature gauge, respectively. H_2S is hydrogen sulfide.

The cylindrical vessel had an inner diameter of 0.425 m, and a length of 1.22 m. The injector and producer wells were perforated stainless-steel tubes. The injector well had a single row of 24 equally spaced perforated holes that are 1.32 mm in diameter and located in the upper side of the tube; this was different from the SAGD experiment in which the injection well was fully perforated in all directions. The injector and producer wells were vertically stacked at 0.12 and 0.04 m from the bottom of the cylindrical pressure vessel and were covered by a stainless-steel mesh to prevent sand production during the experiment. A total of 19 multipoint thermocouple strings were installed on each of the five equally spaced planes shown in **Fig. 2** (i.e., 95 temperature reading points in total). They recorded the real-time temperatures throughout the experiment. The cylindrical vessel was covered with band heaters and ceramic wool to control the heat losses during the experiment.

Fluid Properties. The molecular weight and density of the bitumen were 560 g/mol and 1015 kg/m^3 at 15°C and atmospheric pressure, respectively. Detailed bitumen properties can be found in Appendix A.

The coinjected condensate was prepared with 1.2-mol% methane (C_1), 9.9-mol% butane (n-C_4), 82.4-mol% octane (n-C_8), and 6.5-mol% dodecane (n-C_{12}). The molecular weight of this synthetic condensate was 111 g/mol, and its density was 700 kg/m^3 at 15°C and atmospheric pressure. Bubblepoints of the condensate and several condensate/bitumen mixtures were measured by constant mass expansion. Appendix A gives the fluid experimental data.

Experimental Procedures. ***Model Packing and Oil Saturation.*** The cylindrical vessel was packed and compacted with 312.11 kg of unconsolidated dry sand with the grain size distribution from 0.063 to 0.5 mm with a median of 0.168 mm and an average of 0.183 mm.

The model was evacuated to remove air and check for any leakage after the packing was completed. The model was then saturated with deionized water. The bulk volume and pore volume were measured to be 175.7 (excluding dead volumes) and 58.6 L, respectively. This gave a sandpack porosity of 0.33. The permeability of the sandpack was measured to be 5.6 darcies.

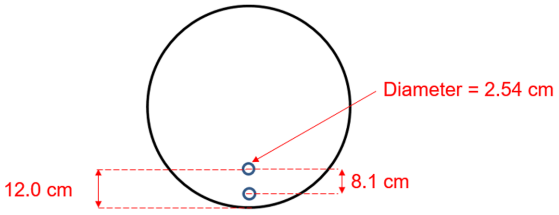

(a) Locations of the horizontal wells on a vertical cross-section.

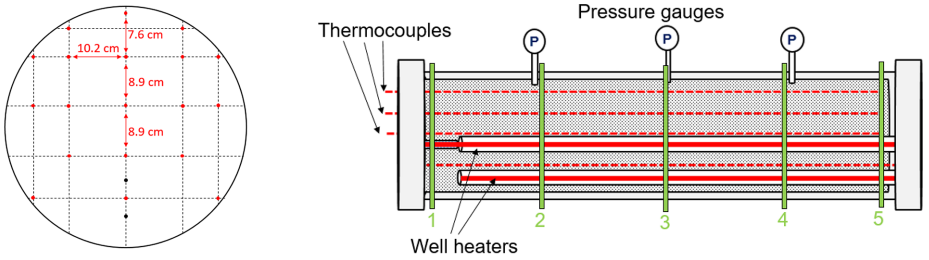

(b) Locations of the thermocouples in the sandpack. (Red dots: thermocouples; black dots: horizontal wells)

Fig. 2—Locations of the horizontal wells and thermocouples in the cylindrical sandpack for the SA-SAGD experiment.

Once the model was fully saturated with water, it was heated to approximately 75°C. Then, heated bitumen was injected into the model, displacing water from the bottom in the gravitationally stable direction. The amount of bitumen injected into the sandpack was 54.7 L, which corresponds to an oil saturation of 93.3%.

Model Preheating. The preheating stage began by turning on the inline heaters of the injector and producer wells. The inline heater temperatures were gradually increased to 125°C and maintained at this setpoint for 24 hours. The heat losses from the cylindrical model were controlled by the top and bottom band heaters.

SA-SAGD Experiment. After 24 hours of preheating, steam was injected into the sandpack at a rate of 50 cm^3/min (cold-water equivalent) at 3500 kPa. After approximately 2.5 hours of steam-only injection for hydraulic communication between the wells, coinjection of condensate with steam was commenced at 2.8 mol%, which corresponded to a rate of 12.5 cm^3/min at 3500 kPa and 8°C. Steam/condensate coinjection continued for 53 hours.

Previous studies using the physical model at Saskatchewan Research Council indicated that it is necessary to control the heat losses from the model by using the band heaters; otherwise, a steam chamber does not start to expand only by the steam injection at a rate that keeps the liquid level above the producer. A steam chamber needs to start expanding early in the experiment so that the oil-recovery data represent multiphase flow along the edge of a steam chamber, instead of (hot) water imbibition.

The heat losses from the model were controlled by using the band heaters on the surface of the experimental vessel to approximate a no-heat-flux boundary. The automatic/real-time control of the band heaters ensured an accurate energy input to the outer boundary of the sandpack. To avoid heating the sandpack by the vessel band heaters, an automated control logic was used for the heaters based on the temperature readings inside the model, closest to the model boundaries (Fig. 2b). In this way, the temperature of the band heaters approximated the temperature inside the model boundary, minimizing the heat flux across the boundary. As will be subsequently shown, however, the calibrated numerical model in this research has indicated that heat losses still occurred; for example, losses occurred from the side boundaries and where the temperature was not measured for controlling the band heaters.

Rampdown/Cooling Stage. After a total of 55 hours of the SA-SAGD stage, the experimental setup was prepared for the winddown/cooling stage. The steam and condensate injection pumps were stopped, the top and bottom band heaters were turned off, and nitrogen was injected into the sandpack at 3500 kPa. The purpose of nitrogen purging was to displace the retained condensate and to remove any hydrogen sulfide (H_2S) in the sandpack for post-run model excavation. The nitrogen purging continued for approximately 8 hours, and all effluent produced during the nitrogen purging was measured and analyzed. Once the nitrogen purging was completed, the model was depressurized from 3500 kPa to near atmospheric pressure over 8 hours.

Handling of Produced Fluids. Two production tanks were alternating for collecting produced fluids. Production tanks were switched every 2 to 3 hours to obtain frequent data of fractional flow and fluid properties. The produced gases and water vapors accumulated in the production tanks were passed through a condenser and a knock-out drain vessel to collect the water and liquid condensate. Dry produced gases were then directed through an inline gas chromatograph for gas compositional analysis, and then through a wet test meter to measure the volumes of the produced gases.

Once a production tank was switched and isolated from the system, the produced liquids were transferred to graduated cylinders from the bottom drain line of the production tanks. Produced liquids were analyzed to measure the amounts of water, condensate, and oil produced. The cumulative amounts of produced oil, water, and condensate were measured and recorded for the entire experiment.

Post-Run Degassing and Model Excavation. Once the SA-SAGD and winddown/cooldown stages were completed, the model was prepared for excavation. The sandpack was excavated from the injection and production ends by dividing the sandpack equally into eight segments along the matrix. Five sand samples were taken from each segment. Samples were analyzed for the contents of sands, water, oil, and asphaltenes.

Experimental Results and Discussion

This section presents the experimental results and their analysis. Comparisons of SA-SAGD with SAGD are discussed based on the SAGD counterpart presented in Sheng et al. (2020b).

Fig. 3a shows the production of total liquid hydrocarbon, which came from two contributions, bitumen (Fig. 3b) and liquid condensate (Fig. 3c) at standard conditions. The final bitumen recovery was 46 034 cm^3 (Fig. 3b) or 84.1% of the original oil in place. The recovery factor was 73.3% at 2,880 minutes after the start of the preheating (i.e., one day of steam injection), and 82.9% at approximately 3,600 minutes. The production rate changed at approximately 3,000 minutes in Fig. 3a, which came from the bitumen depletion as shown in Fig. 3b. The solvent recovery reached 87% at the end of the solvent injection stage, and 95% at the end of the experiment (after nitrogen purging and matrix pressure depletion stages). In general, such a large recovery factor of solvent may not be expected in the field application because of various complexities and uncertainties in actual reservoirs, such as heterogeneous petrophysical properties and the scale-dependent mixing of solvent with bitumen.

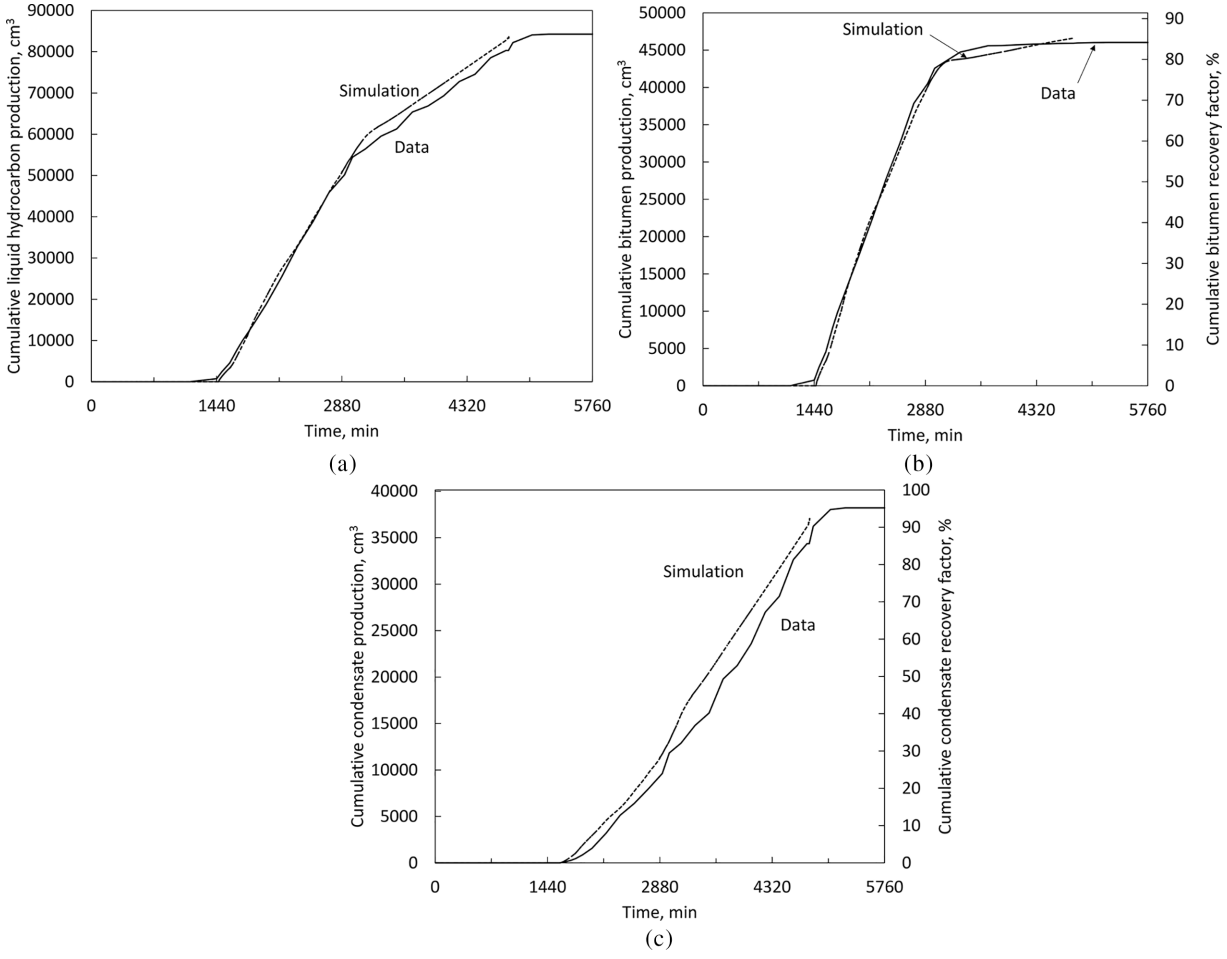

Fig. 3—Cumulative liquid hydrocarbon production from the experimental data and the calibrated SA-SAGD simulation at standard conditions: (a) liquid hydrocarbon production at standard conditions, (b) bitumen production at standard conditions, and (c) liquid condensate production at standard conditions.

Table 1 gives the volume balance for water, bitumen, and condensate at standard conditions. The amounts remaining in the sandpack were estimated from the excavated samples. Although the material balance was satisfied reasonably for bitumen and condensate, Table 1 shows that 3.9 L of water was lost **(Fig. 4).** The lost volume can be affected by the uncertainty in the estimated volume retained in the sandpack because the distribution of water in the sandpack was uncertain after being cooled down and purged with nitrogen. Also, water and bitumen could be lost during the handling of produced fluids, especially emulsions.

			Production			
	Original in Place	Injection	Liquid	Gas (Liquid Equivalent Volume)	Retention in Sandpack	Lost Volume
Water	4.89	170.3	158.41	0	12.93	3.89
Bitumen	54.73	0	46.05	0	6.44	2.26
Condensate	0	40.2	38.66	0.64	0.48	0.37

Table 1—Volume balance at standard conditions for the SA-SAGD experiment for water, bitumen, and condensate. All numbers are in liters. The amounts of retention in the sandpack were estimated by using the data from excavated samples.

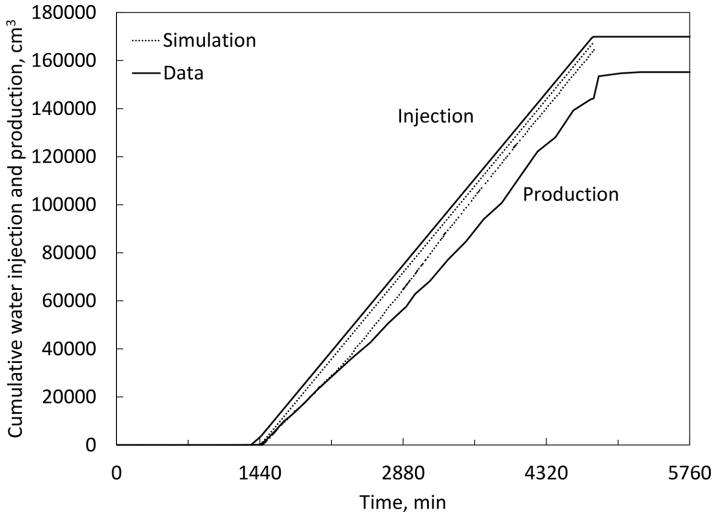

Fig. 4—Cumulative water injection and production histories in the SA-SAGD experiment and the calibrated SA-SAGD simulation at standard conditions.

Although the measured SOR at the laboratory-scale SA-SAGD does not represent a field-scale process, **Fig. 5a** shows the cumulative SOR for the SAGD and SA-SAGD experiments. The SOR in this figure was calculated by the volume of the injected steam (cold-water equivalent) divided by the volume of the bitumen produced. The SA-SAGD experiment in this research resulted in two to three times smaller cumulative SOR than the SAGD experiment. As mentioned in "Experimental Procedures," the heat-loss control was to represent a no-heat-flux boundary in the experiments. That is, the cumulative SORs given in Fig. 5a were compared based on the controlled heat loss boundary at the scale of the experiments.

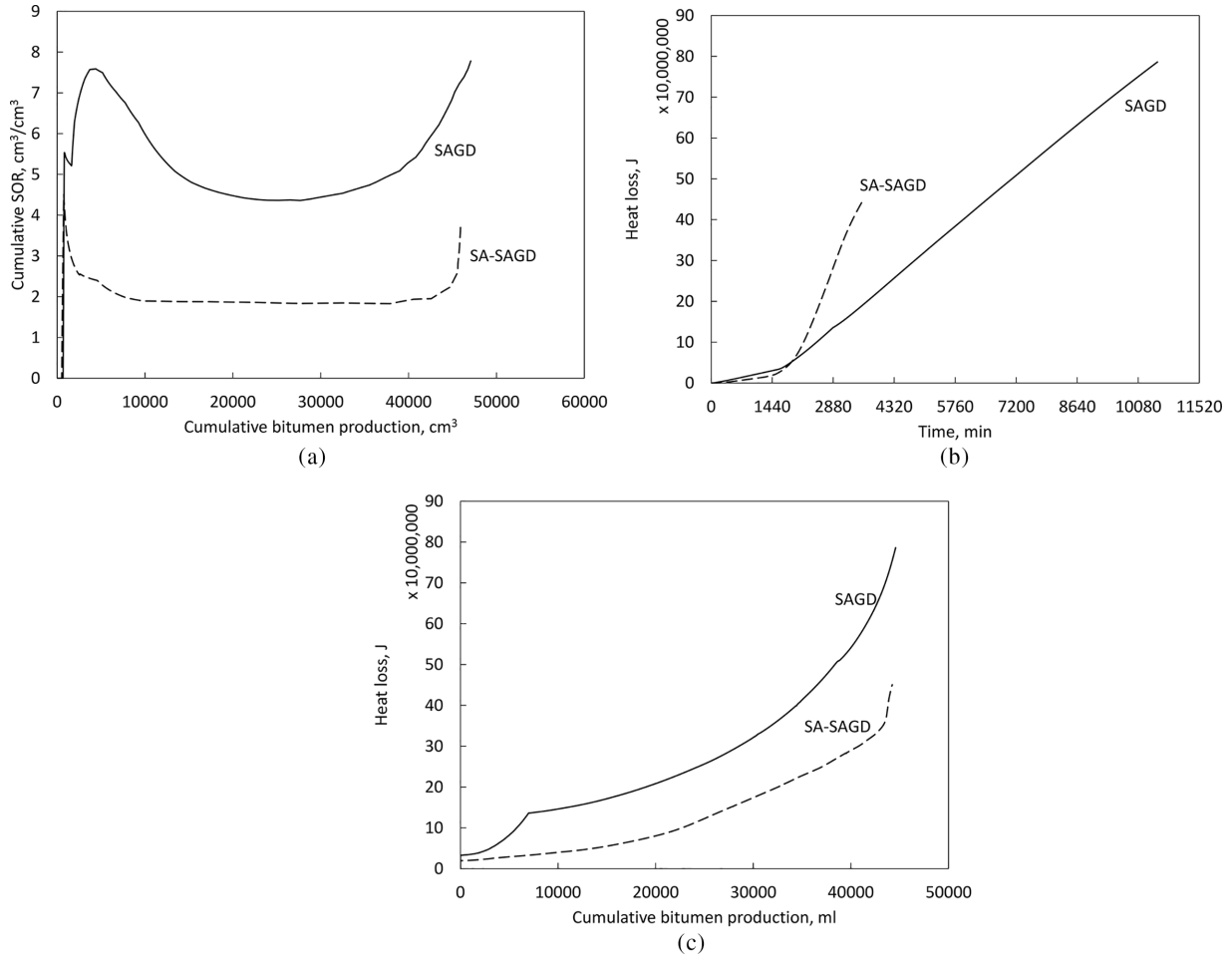

Fig. 5—Comparison of the SAGD (Sheng et al. 2020b) and SA-SAGD experiments in terms of energy efficiency: (a) cumulative SOR from the experiments, (b) estimation of the heat loss with respect to time based on the history-matched simulation models, and (c) estimation of the heat loss with respect to bitumen production based on the history-matched simulation models.

The SAGD cumulative SOR could have been underestimated because a detailed analysis indicated that the energy input through the wellbores was greater in SAGD than in SA-SAGD. Possible reasons for a smaller SOR of SA-SAGD than SAGD are given in the literature (Nasr et al. 2003; Dong 2012), and they are also confirmed through the history-matched simulation models in this research. One reason is that the injected solvent facilitates oil production and, therefore, reduces the heat losses by reducing the exposure time of a high-temperature chamber to the surroundings. Another reason is that the volatile solvent reduces the condensation temperature of steam and, therefore, can reduce the heat losses. In Figs. 5b and 5c, the heat losses from the experiments were estimated by the history-matched simulation models to be shown in the next section. SA-SAGD took a much shorter time to deplete the sandpack and eventually caused less heat loss than SAGD.

Fig. 6 (the middle column) shows temperature contours for the second vertical plane from the injection side before 3,600 minutes, when the bitumen production became nearly the final value. The temperature contours were constructed by fitting a 3D surface with the 103 thermometer readings indicated by the small circles in Fig. 6. The five contours represent 180, 195, 210, 225, and 240°C. Only the second vertical plane was presented here because the first and fifth were in contact with the metal flanges, and the temperature information was not indicative of the sandpack. Also, the temperatures on the third and fourth planes were very similar to the second plane, indicating the uniform propagation of a steam chamber. Unlike the SAGD experiment, the temperatures near the edge of an SA-SAGD steam chamber were sensitive to the local fluid compositions; therefore, it was not possible to indicate the expansion of a steam chamber based on the temperature profiles. The temperature contours, however, were useful for history matching, as will be presented in the next section.

Fig. 7a shows the densities measured for the 10 produced oil samples (mixtures of the produced condensate and bitumen) collected at different times after they were separated from water. The density of the produced oil gradually reduced from 1000 kg/m^3 at the beginning to 750 kg/m^3 at the end of the experiment. This occurred because the amount of condensate increased in the produced hydrocarbon, which reduced the relative amount of asphaltene in the produced oil, as shown in Fig. 7b. The produced oil properties were effectively used for the history matching in the next section.

The sandpack was divided into eight equally spaced segments after the experiment, and five samples were taken from each segment for asphaltene analysis. **Fig. 8** shows photos of the excavated sandpack after the experiment. **Table 2** and **Fig. 9** report the results of the successfully taken samples. The sandpack after the experiment clearly showed two regions with different colors: one with light color near the vessel's wall contained the other dark region. The asphaltene analysis indicated that the samples taken from clean parts had a negligible amount of asphaltene, which will be also explained by the history-matched simulation in the next section. Those from dark parts showed the asphaltene content that was approximately 6 wt% greater than that of the original bitumen, 17.82 wt%. This indicates that the light components of bitumen were vaporized. The samples taken partly from the dark and clean zones showed asphaltenes content ranging from 12 to 19 wt%.

The recovery factor of asphaltenes was calculated by dividing the total asphaltene production by the original asphaltene in place. The produced asphaltene for SA-SAGD can be estimated by using volumetric production data in Fig. 3, the density data in Fig. 7a, and the asphaltene concentration in the produced bitumen in Fig. 7b. The same calculation can be done for SAGD data. The result shows that SA-SAGD recovered 85.4% of the original asphaltene in place at the end of the experiment, in comparison to 73.6% in the SAGD experiment. In-situ upgrading in SAGD occurred due to distillation of the light-ends in bitumen and aquathermolysis. The higher asphaltene recovery factor in SA-SAGD indicates a lower level of aquathermolysis and a greater displacement efficiency by solvents, as will be explained in the next section.

The concentration of H_2S in the effluent gas samples was monitored for safety purposes using gas chromatography. The H_2S concentration data were also useful to understand the extent of aquathermolysis (Ovalles 2019). It was approximately 0.27 L by the end of the experiment, which was five times smaller than the amount measured from the SAGD experiment using similar operating conditions. Ovalles (2019) stated that the amount of H_2S from aquathermolysis becomes greater with increasing reaction temperature and exposure time of asphaltenes to steam. Temperatures near the SA-SAGD chamber edge were simulated to be 20 to 40°C lower than those in the SAGD experiment, as indicated by the history-matched simulation in the next section. The experimental time was also much shorter for the current SA-SAGD than SAGD.

History Matching and Analysis

History Matching. The SA-SAGD experimental data were history matched with a numerical simulation model by using STARS^{TM} (Computer Modelling Group 2018). The simulation model considered three-phase capillary pressure to allow for the mixed flow regimes of countercurrent and cocurrent flow with an expanding steam chamber. The history-matching process largely followed the history matching of the SAGD experiment (Sheng et al. 2020b).

Two main steps were iteratively taken to match the SA-SAGD results. First, the temperature profiles were matched by adjusting heat-loss parameters. Then, the injection and production histories of water and hydrocarbons were matched by adjusting relative permeability curves. Other parameters, such as permeability, porosity, initial saturations, and fluid properties, were determined via separate experiments as given in the Experimental Method section and Appendix A; that is, they were not adjusted during the history-matching process. The capillary pressures were initiated with the interfacial tensions (IFTs) to be 30 and 15 dynes/cm for water/oil and oil/gas as in the SAGD simulation and updated before each iteration of the two steps. The history matching was performed for the period before 3,600 minutes when the bitumen recovery plateaued as shown in Fig. 3b.

The sandpack was modeled as an approximate cylinder using 5,525 rectangular gridblocks. It had 17 gridblocks for the diameter and 25 gridblocks along the wellbore (J direction). The dimensions of each gridblock were $0.025 \times 0.0488 \times 0.025$ m ($I \times J \times K$).

The fluid model consisted of four condensate components, C_1, n-C_4, n-C_8, and n-C_{12}, and two bitumen components, a distillable component, B1, and a nondistillable component, B2. The fluids were characterized by the Peng-Robinson equation of state (PR EOS; Robinson and Peng 1978) based on bubblepoints for four mixtures of condensate/bitumen (Appendix A). The viscosity and density of bitumen/condensate mixtures were also measured and modeled using STARS fluids models, as also given in Appendix A.

The thermal conductivities of the sand, water, oil, and gas phases were 1.23, 0.36, 0.072, and 0.02 J/(cm min °C), respectively. These parameters were fixed for history matching. Three sets of heat-loss parameters were used for the injection-end flange, the production-end flange, and the sandpack as given in **Table 3.** These values were similar to the heat-loss parameters used for the chamber-expansion period in the SAGD experiment (referred to as "Period 2"), because the heat losses were controlled similarly in these experimental periods. A single set of heat-loss parameters was used for the entire sandpack, because the temperature distribution along the wellbore was nearly uniform as mentioned previously. As in the SAGD experiment, heat-loss parameters were required to obtain a reasonable match of temperature distribution data. That is, despite the effort to control the heat losses with the band heaters, a certain level of heat losses still occurred in the experiments. However, similar heat loss parameters were used for SA-SAGD and SAGD, making it possible to compare the two comparative experiments.

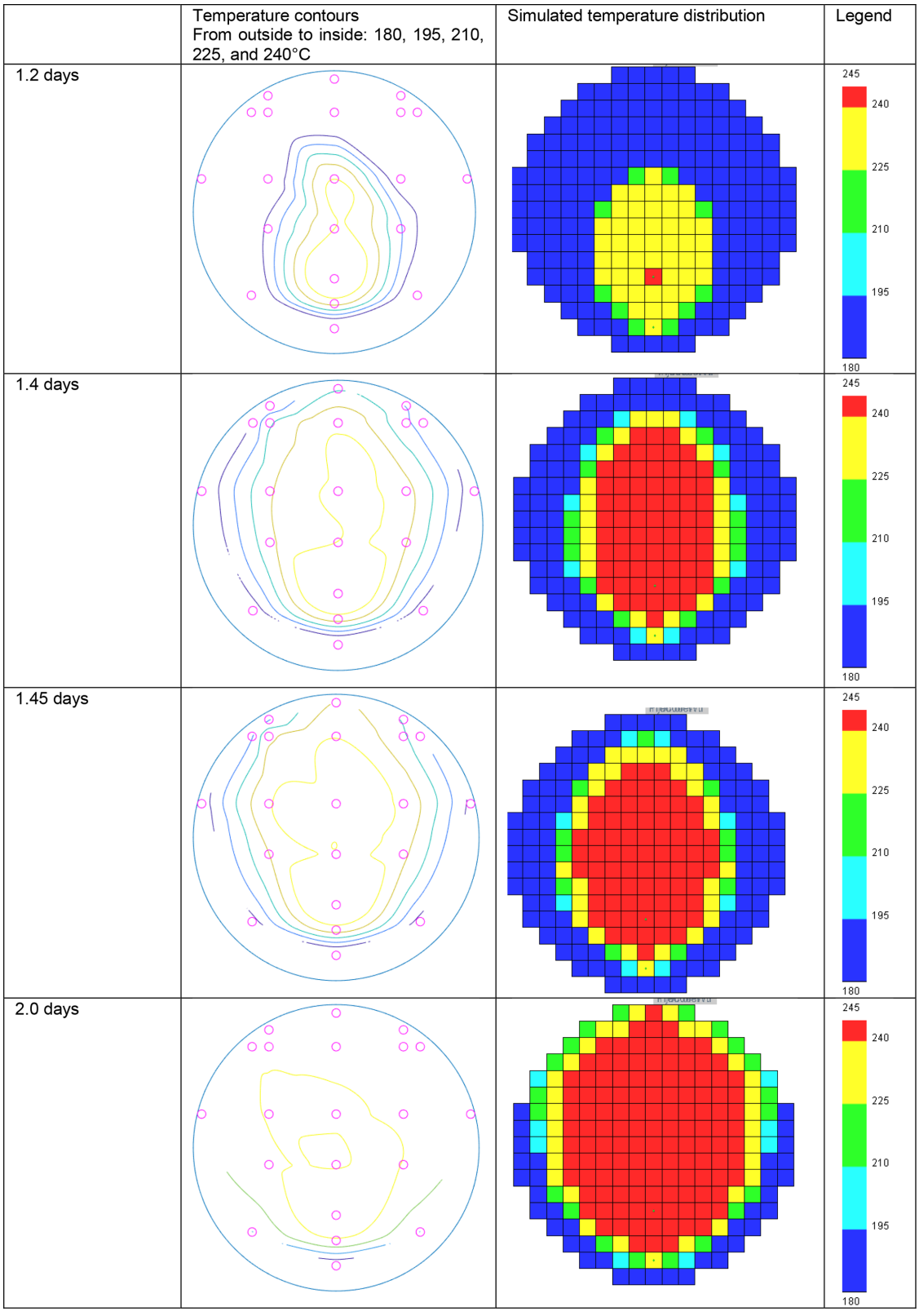

Fig. 6—Temperature profiles on the second plane from the injection side in the SA-SAGD experiment and in the calibrated SA-SAGD simulation.

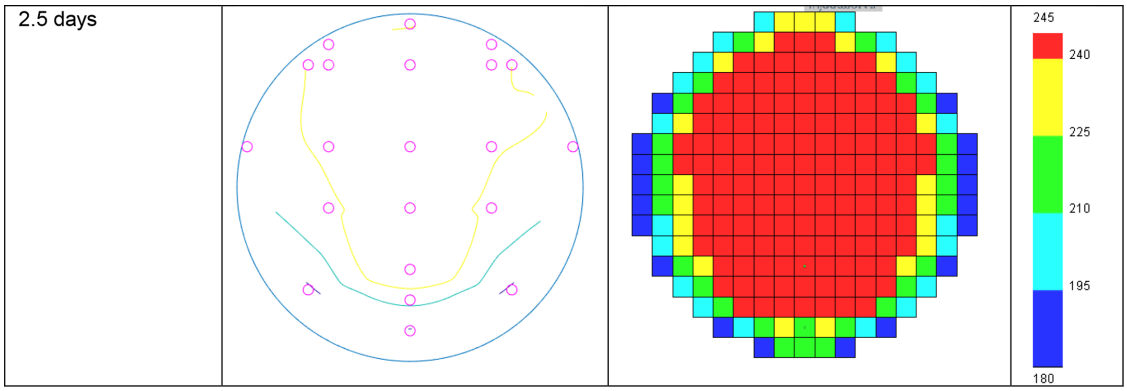

Fig. 6 (continued)—Temperature profiles on the second plane from the injection side in the SA-SAGD experiment and in the calibrated SA-SAGD simulation.

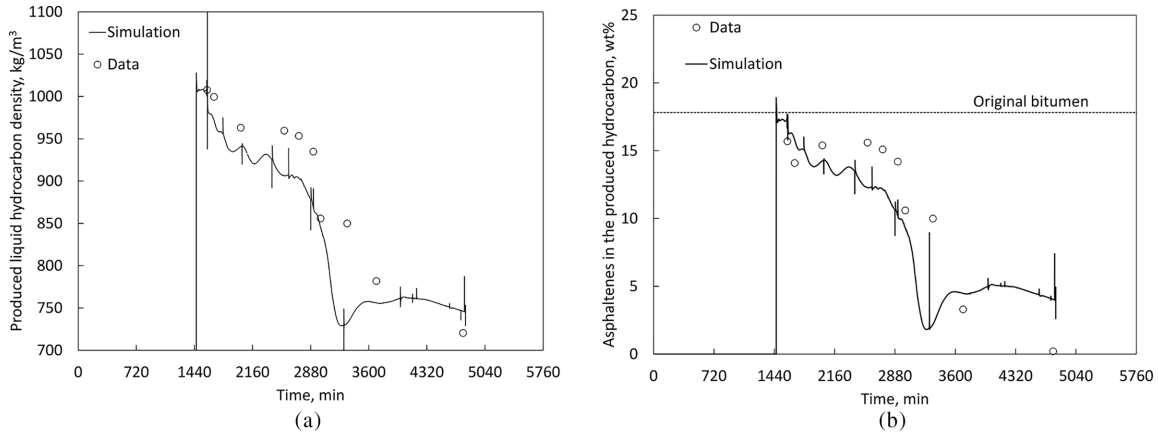

Fig. 7—Produced oil properties from the SA-SAGD experiment and the calibrated SA-SAGD simulation: (a) produced liquid hydrocarbon density and (b) produced asphaltenes content in the hydrocarbon.

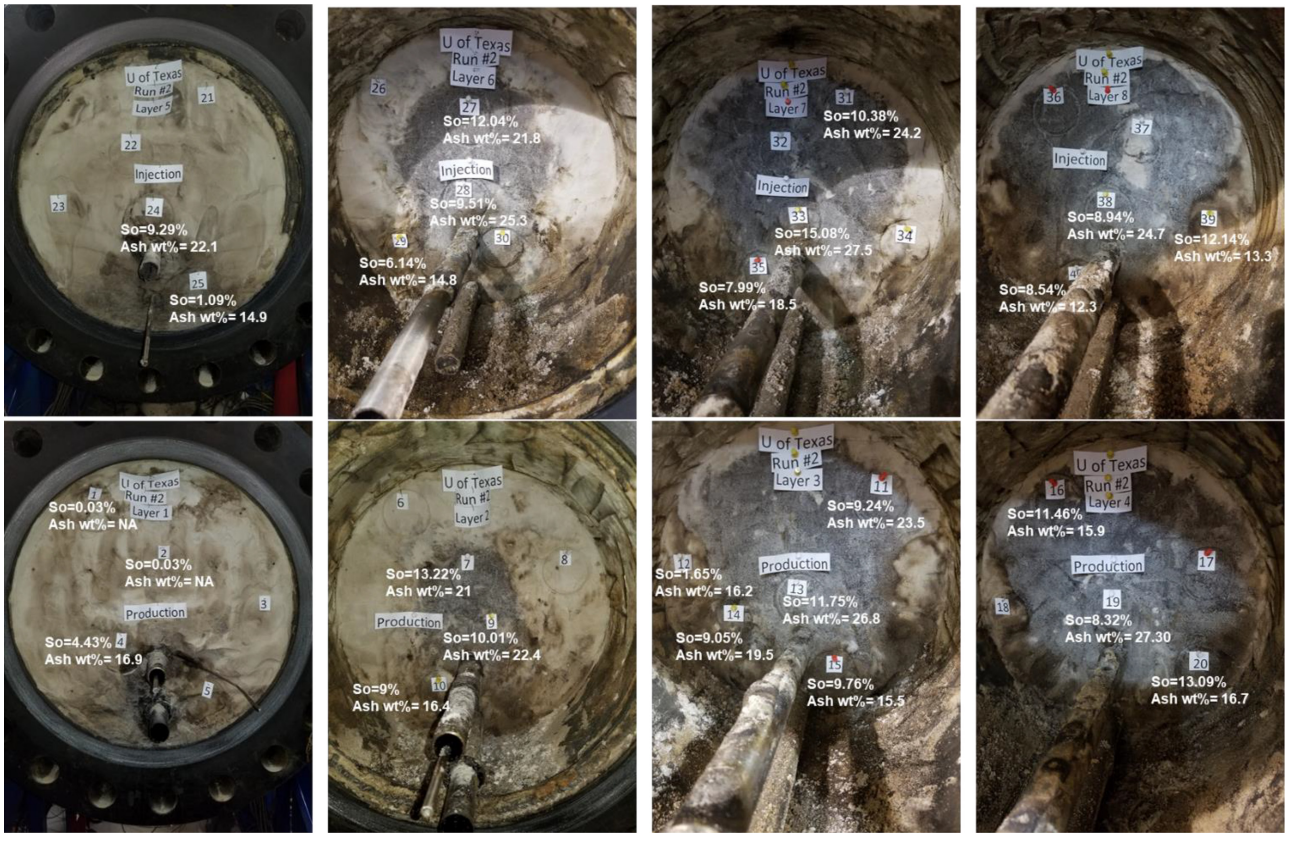

Fig. 8—Photos of the sandpack after the SA-SAGD experiment. The four pictures at the top are on the injection side, and the four pictures at the bottom are on the production side.

Sample Number	Asphaltenes (wt%)	Zone
	Production End	
1	N/A	Clean
2	N/A	Clean
4	16.9	Transition
7	21	Dark
9	22.4	Dark
10	16.4	Transition
11	23.5	Dark
12	16.2	Transition
13	26.8	Dark
14	19.5	Transition
15	15.5	Transition
16	15.9	Transition
19	27.3	Dark
20	16.7	Transition
	Injection End	
4	22.1	Dark
5	14.9	Transition
7	21.8	Dark
8	25.3	Dark
9	14.8	Transition
11	24.2	Dark
13	27.5	Dark
15	18.5	Transition
18	24.7	Dark
19	13.3	Transition
20	12.3	Transition

Table 2—Asphaltene concentration in the remaining oil after the SAGD experiment. The third column was made based on the observation from excavated samples (Fig. 8). “Clean” and “dark” means that the sample was taken where the sand color was light and dark, respectively. “Transition” indicates that the location was partially “clean” and “dark.”

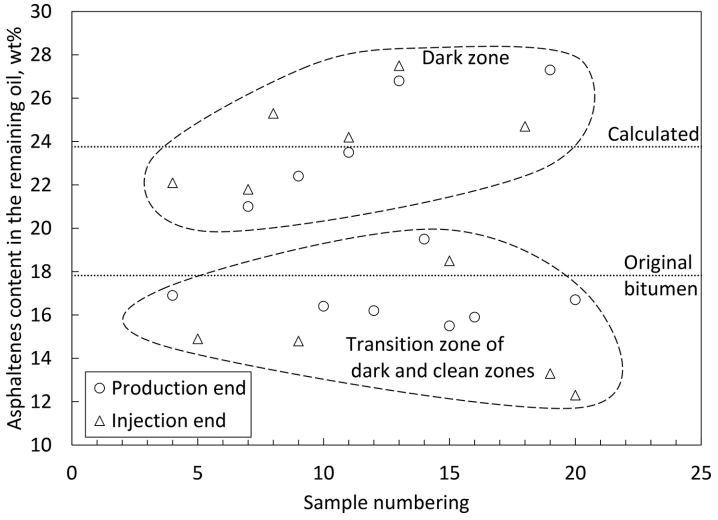

Fig. 9—Asphaltene wt% in the excavated samples. “Dark zone” and “transition zone” indicate sampling locations in the dark sand, and in the boundary between clean and dark sands in Fig. 8. “Calculated” indicates the asphaltene content in the residual oil by assuming asphaltene is completely in B2 and B1 is vaporized.

	Flanges—Injection End	Flanges—Production End	Sandpack
Heat conductivity in *I*, [J/(cm min °C)]	–	–	7.0
Heat capacity in *I*, [J/(cm min °C)]	–	–	2.0
Heat conductivity in *J*, [J/(cm min °C)]	0.05	0.10	–
Heat capacity in *J*, [J/(cm min °C)]	0.25	0.25	–
Heat conductivity in +*K*, [J/(cm min °C)]	0.03	0.20	4.0
Heat capacity in +*K*, [J/(cm min °C)]	0.02	0.02	2.0
Heat conductivity in –*K*, [J/(cm min °C)]	0.02	0.15	2.0
Heat capacity in –*K*, [J/(cm min °C)]	0.02	0.02	2.0

Table 3—Heat-loss parameters for the calibrated SA-SAGD simulation. *I*, *J*, +*K* and –*K* are the directions perpendicular to the well pair, along the well pair, underburden, and overburden, respectively.

Figs. 3 and 4 compare the material balance for hydrocarbon and water from the simulation with the SA-SAGD experimental data. They show a reasonable agreement between the simulation and the experimental data before 3,600 minutes, except for the water production data (Table 1). Fig. 6 (the right column) shows that the temperature profiles on the second vertical plane from the injection side were reasonably matched before 3,600 minutes.

Simulated Flow Regimes. Fig. 10 compares the profiles for SA-SAGD with those for SAGD when the bitumen production was 25 000 cm^3. Figs. 10a through 10c show that SA-SAGD had a much greater steam chamber than SAGD for the same bitumen production; that is, the water saturations outside the steam chamber were much smaller in SA-SAGD than in SAGD. Sheng et al. (2020b) presented that the oil recovery in their SAGD experiment occurred outside the steam chamber by the displacement by liquid water, initially countercurrently and later cocurrently. Although the countercurrent flow of water and oil can recover oil, the progressively increasing amount of water outside the steam chamber tended to reduce the amount of oil to be heated and also did not act as a carrier for bitumen components. The SA-SAGD case could expand the chamber much more easily because the volatile components tended to remain in the vapor phase and because the condensed solvent increased the bitumen mobility as a miscible carrier without needing a lot of water throughput.

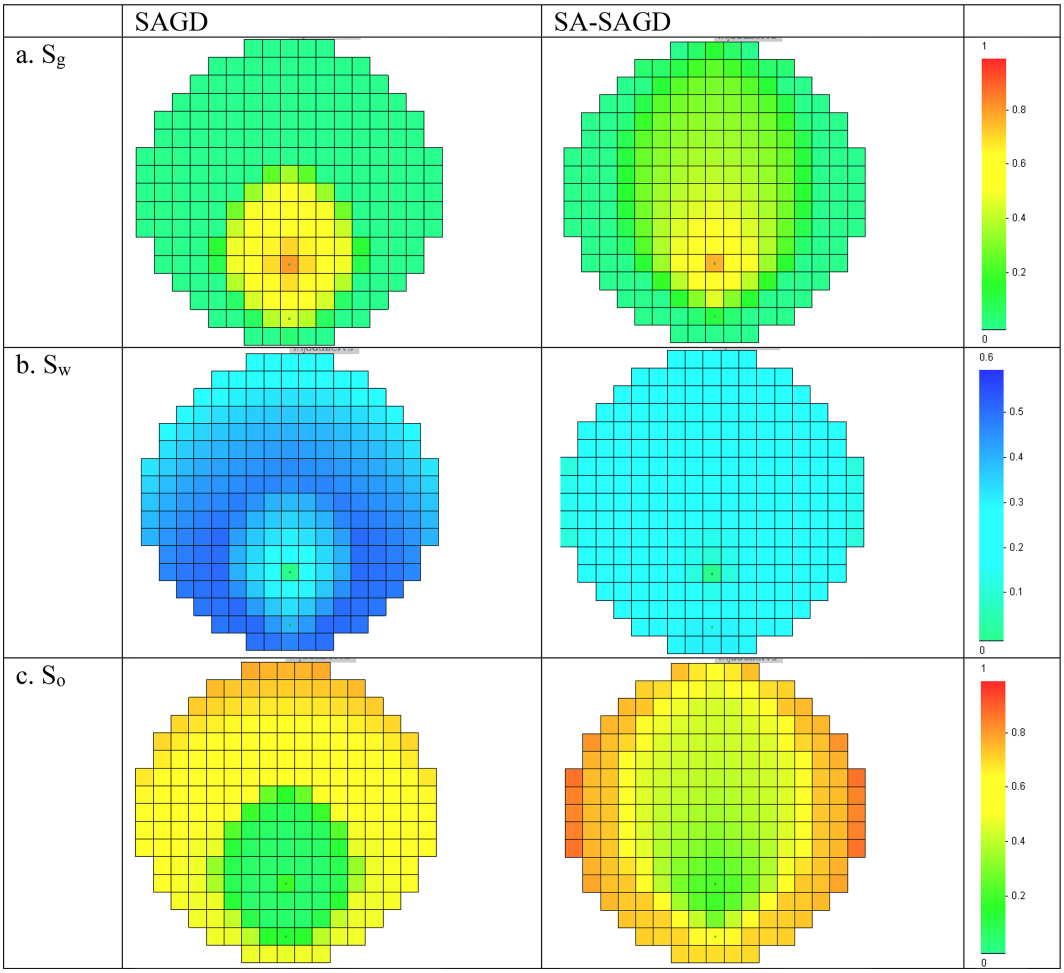

Fig. 10—Simulated profiles of SAGD and SA-SAGD when bitumen production was 25 000 cm^3.

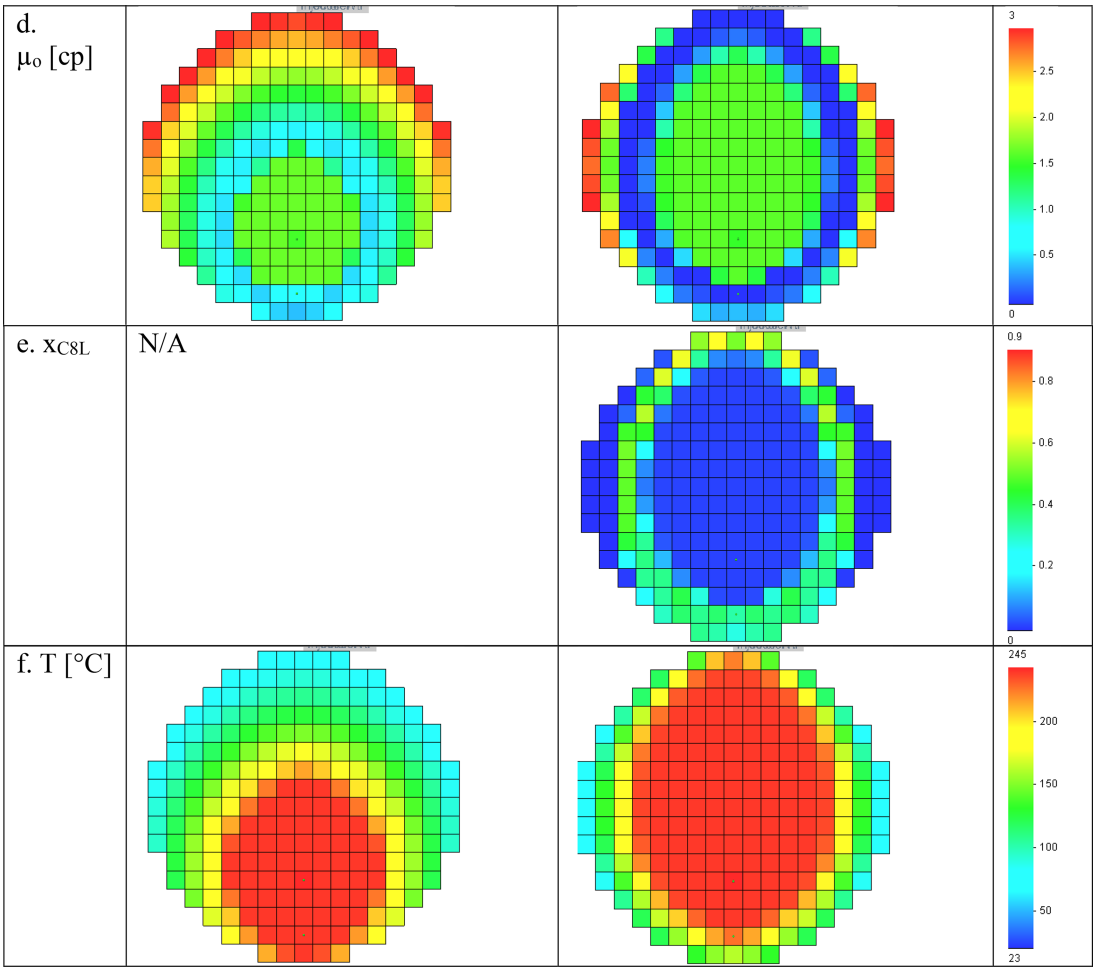

Fig. 10 (continued)—Simulated profiles of SAGD and SA-SAGD when bitumen production was 25 000 cm^3.

Sheng et al. (2020b) pointed out the importance of considering capillary pressures to obtain a reasonable history match in steam-chamber expansion behavior for their SAGD experiment. In the case of SA-SAGD, it was necessary to make the capillary pressures (**Fig. 11**) smaller than those for SAGD; this particularly helped the simulation model represent a rapid expansion of the SA-SAGD chamber vertically. The resulting IFTs between oil/water and oil/gas were 18 and 4.5 dynes/cm to give the best match of temperature and production histories. The lowered IFT in SA-SAGD was conceivable because the partitioning of condensate in the oleic and vapor phases should have lowered the IFTs, as indicated in the literature (Das 1998; Mendoza de la Cruz et al. 2009; Mohammadi et al. 2020). The lowered water/oil and gas/oil capillary pressures tended to suppress the countercurrent flow of water and oil that was less efficient in oil recovery from outside of the steam chamber (Fig. 10a) than cocurrent flow. As subsequently explained, cocurrent flow of oil and water tended to make the oil recovery in SA-SAGD more rapid and the SOR smaller than the SAGD experiment.

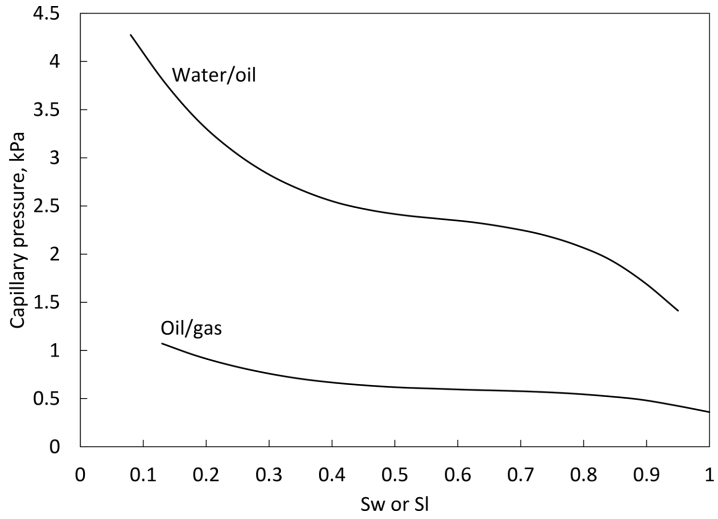

Fig. 11—Capillary pressure curves used for the calibrated SA-SAGD simulation model. The IFT between oil and water is 18 dynes/cm, and that between liquid and gas is 4.5 dynes/cm.

The relative permeabilities **(Fig. 12)** resulting from the history matching were much greater from those for the SAGD experiment likely because these two experiments had different flow regimes. The flow regimes in the SAGD and SA-SAGD experiments were compared through the calibrated simulation models. The angle between oil and water flow vectors was quantified by θ; the oil and water phases flow in the same direction when $\cos\theta$ is unity (completely cocurrent); the oil and water fluxes are in the opposite direction (completely countercurrent) when $\cos\theta$ is -1. **Fig. 13** shows $\cos\theta$ for SAGD and SA-SAGD at a few different amounts of bitumen production. The SAGD case switched the predominant flow regime from countercurrent to cocurrent flow, as shown by the reduced cold-color area in the first column of Fig. 13. The SA-SAGD case, in contrast, shows that the countercurrent flow was limited to a very small region at the early times.

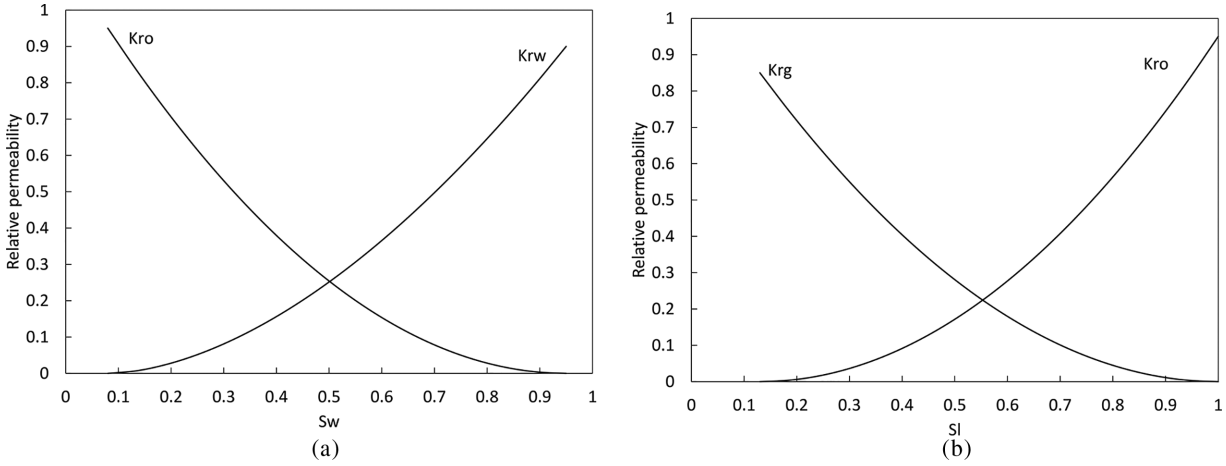

Fig. 12—Two-phase relative permeability models for Stone 1 model for the history-matched SA-SAGD simulation model: (a) water/oil relative permeabilities and (b) oil/gas relative permeabilities.

The water/oil cocurrent flow seems to have dominated in the SA-SAGD experiment, which is consistent with the water/oil relative permeability (Fig. 12). **Table 4** compares the parameters in the Corey models for the SA-SAGD case and the SAGD case. The current SA-SAGD case required greater water/oil and oil/gas relative permeabilities than the two periods in the SAGD case. Previous studies suggested that greater relative permeabilities should be used for cocurrent flow than countercurrent flow (Bourbiaux and Kalaydjian 1990; Kalaydjian 1990; Bentsen and Manai 1993; Haugen et al. 2015; Andersen et al. 2020). Fig. 9 also shows that the oil viscosity was significantly reduced by condensate in the SA-SAGD case. The lowered oil/water viscosity ratio might have also contributed to the predominantly cocurrent flow in the SA-SAGD case.

Estimation of Asphaltenes Content in Produced Oil and Remaining Oil

Although the oil recovery started to plateau approximately at 3,600 minutes, the simulation until 4,800 minutes assisted the analysis of the produced oil properties and excavated oil samples. Fig. 7a shows that the simulated density was in good agreement with the experimental data.

The asphaltenes content in the produced oil and remaining oil were calculated by using the simulation results, in which asphaltenes were assumed to reside only in the B2 component (nondistillable). Fig. 7b shows that this asphaltene assignment gave a reasonable match of asphaltene content in the produced oil during the SA-SAGD experiment. This assumption also resulted in a reasonable match in asphaltene concentration in the remaining oil; Fig. 9 shows that the data points from the dark parts were reasonably represented by the calculated value, 23.75 wt%, with the asphaltene content assigned only to B2.

Fig. 14 shows the simulated C_8 and B2 concentrations in the remaining oil at 4,800 minutes with the calibrated simulation model. Fig. 10f showed that temperatures near the interior wall could be much lower than the center of the sandpack, and the solvent components tended to accumulate along the wall as shown in Fig. 14a (C_8 in this figure as an example). Fig. 14b shows that the B2 concentration was simulated to be much smaller near the wall than near the center of the sandpack, where the remaining oil consisted of nearly 100% B2. The distribution of B2 in the simulation is in line with the photo shown in Fig. 8 (Layer 7 is close to the cross section shown in Fig. 14).

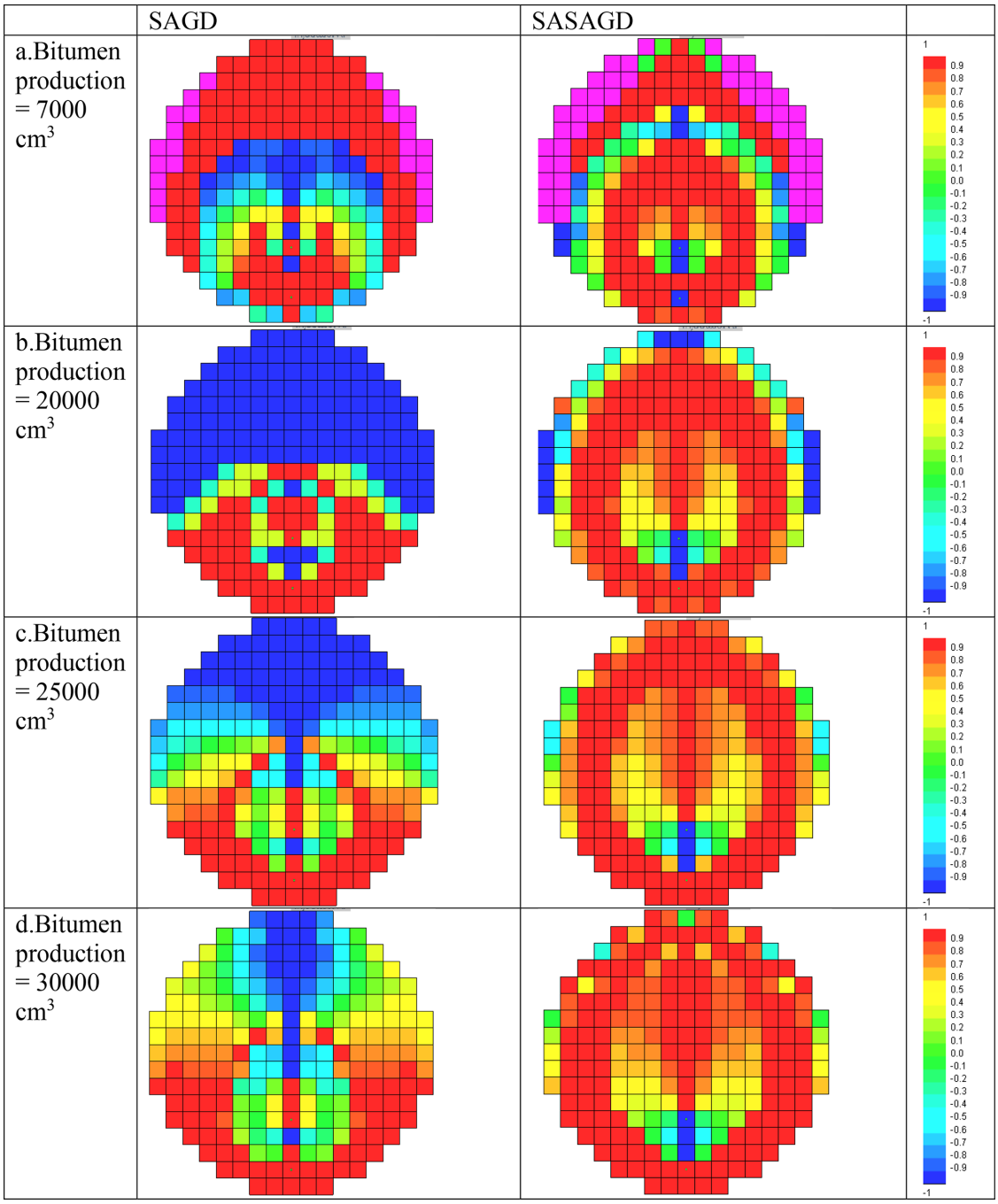

Fig. 13—Cosine of the angle between the water and oil fluxes. The two phases flow in the same direction (completely cocurrent) when the value is unity, and in the opposite direction (completely counter current) when the value is –1.

Parameters	SA-SAGD in This Research	SAGD Period 1 in Sheng et al. (2020b)	SAGD Period 2 in Sheng et al. (2020b)
S_{wr}	0.07	0.07	0.07
S_{or} (oil/water, oil/gas)	0.05	0.05	0.05
S_{gr}	0	0	0
K_{ro} ($S_w = S_{wr}$)	0.95	0.20	0.95
K_{rw} ($S_w = 1 - S_{or}$)	0.90	0.025	0.05
K_{rg} ($S_l = 1 - S_{gr}$)	0.85	0.125	0.20
Exponent, K_{rw}	1.75	2.75	2.5
Exponent, K_{ro}	2.0	2.75	1.4
Exponent, K_{rg}	2.0	4.5	4.5

Table 4—Relative permeability parameters for the three-phase Stone-1 model after history matching. Period 1 refers to the early stage of steam injection in the SAGD experiment (Sheng et al. 2020b) whereby the bottom band heater was not used. Period 2 refers to the later stage of the SAGD experiment whereby the bottom band heater was used.

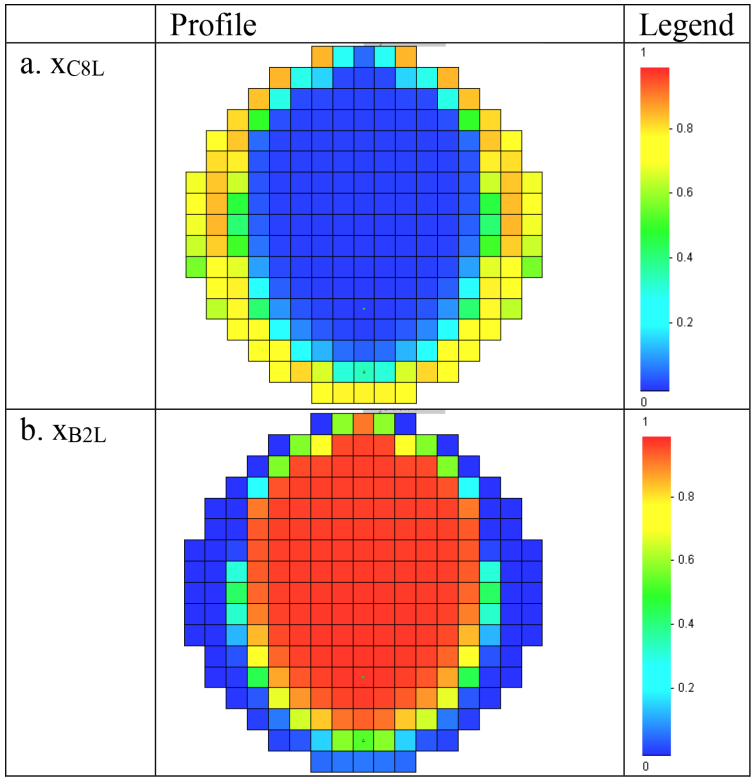

Fig. 14—Mole fractions of C_8 and B2 in the oleic phase at 4,800 minutes from the calibrated numerical simulation. The cross section shown in this figure is close to Layer 7 in Fig. 8.

Conclusions

In this paper, we presented an experimental study of SA-SAGD with multicomponent solvent (i.e., condensate) using a large physical model. The cylindrical model had a diameter of 0.425 m, a length of 1.22 m, a porosity of 0.33, and an average permeability of 5.6 darcies. The SA-SAGD experiment was performed at 50 cm^3/min (cold-water equivalent) with the condensate concentration of 2.8 mol% at 3500 kPa. The condensate used for the experiment was a mixture of C_1, n-C_4, n-C_8, and n-C_{12}. The experimental data were history matched by a numerical simulation model in terms of the material balance of water, bitumen, and condensate and temperature distribution. The main conclusions are as follows:

1. The cumulative SOR calculated by the volume of the injected steam (cold-water equivalent) divided by the volume of the bitumen produced in the SA-SAGD experiment was two to three times smaller than the SAGD experiment by Sheng et al. (2020b). Experimental and numerical results indicated that SA-SAGD could expand the steam chamber more efficiently than SAGD. The more efficient expansion of the SA-SAGD chamber occurred because the volatile hydrocarbons tended to remain in the vapor phase and because the condensed solvent increased the bitumen mobility as a miscible carrier without needing a lot of water throughput. Water does not effectively act as the volatile component that keeps a vapor chamber and once condensed, it does not act as an effective carrier for bitumen components in either SAGD or SA-SAGD.
2. The relative permeabilities resulting from the history matching were quite different from those for the SAGD experiment likely because these two experiments had different flow regimes. Detailed analysis of the calibrated simulation models indicated that the water/oil cocurrent flow dominated in the SA-SAGD experiment, unlike in the SAGD experiment.

3. History matching the experimental data (especially temperature data) required reducing the IFTs between water/oil and gas/oil for SA-SAGD in comparison to those for SAGD. This was likely because the condensate had lowered the IFTs by partitioning in the oleic and vapor phases.
4. Experimental and numerical results showed that the SA-SAGD experiment in this research produced a larger fraction of asphaltene from the original bitumen than the SAGD experiment. In-situ upgrading in SAGD was attributed to the distillation of volatile bitumen components and aquathermolysis. However, both mechanisms were likely suppressed in the SA-SAGD experiment in this research because SA-SAGD resulted in lower chamber temperatures and a shorter production period. Indeed, the H_2S production in the SA-SAGD experiment was negligible. Also, the more efficient displacement of bitumen in SA-SAGD contributed to the increased production of asphaltene components in comparison to SAGD.

Nomenclature

f_i = weighted fraction of a component i in the STARS viscosity model, dimensionless
k_r = relative permeability, dimensionless
P = pressure, kPa
q_i = weighting factor of component i in the STARS viscosity model, dimensionless
T = temperature, °C
x_{iL} = mole fraction of component i in the oil phase
α = fitting parameters for pure component density model in STARS
μ = viscosity, cp
ρ = density, kg/m^3

Acknowledgments

We gratefully acknowledge Japan Canada Oil Sands Ltd. and China National Offshore Oil Corporation International Ltd. for sponsoring this research. Ryosuke Okuno holds the Pioneer Corporation Faculty Fellowship in the Hildebrand Department of Petroleum and Geosystems Engineering at the University of Texas at Austin.

References

Al-Murayri, M. T., Maini, B. B., Harding, T. G. et al. 2016a. Cracked Naphtha Coinjection in Steam-Assisted Gravity Drainage. *Energy Fuels* **30** (7): 5330–5340. https://doi.org/10.1021/acs.energyfuels.5b02773.

Al-Murayri, M. T., Maini, B. B., Harding, T. G. et al. 2016b. Multicomponent Solvent Co-Injection with Steam in Heavy and Extra-Heavy Oil Reservoirs. *Energy Fuels* **30** (4): 2604–2616. https://doi.org/10.1021/acs.energyfuels.5b02774.

Andersen, P. Ø., Nesvik, E. K., and Standnes, D. C. 2020. Analytical Solutions for Forced and Spontaneous Imbibition Accounting for Viscous Coupling. *J Pet Sci Eng* **186:** 106717. https://doi.org/10.1016/j.petrol.2019.106717.

Ayodele, O. R., Nasr, T. N., Beaulieu, G. et al. 2009. Laboratory Experimental Testing and Development of an Efficient Low Pressure ES-SAGD Process. *J Can Pet Technol* **48** (9): 54–61. PETSOC-09-09-54. https://doi.org/10.2118/09-09-54.

Baek, K., Okuno, R., Sharma, H. et al. 2019a. Oil-in-Water Emulsification of Athabasca Bitumen with Pyrrolidine Solution. *Fuel* **246:** 425–442. https://doi.org/10.1016/j.fuel.2019.02.123.

Baek, K., Sheng, K., Argüelles-Vivas, F. J. et al. 2019b. Comparative Study of Oil-Dilution Capability of Dimethyl Ether and Hexane as Steam Additives for Steam-Assisted Gravity Drainage. *SPE Res Eval & Eng* **22** (3): 1030–1048. SPE-187182-PA. https://doi.org/10.2118/187182-PA.

Bentsen, R. G. and Manai, A. A. 1993. On the Use of Conventional Cocurrent and Countercurrent Effective Permeabilities to Estimate the Four Generalized Permeability Coefficients which Arise in Coupled, Two-Phase Flow. *Transp Porous Media* **11** (3): 243–262. https://doi.org/10.1007/BF00614814.

Bourbiaux, B. J. and Kalaydjian, F. J. 1990. Experimental Study of Cocurrent and Countercurrent Flows in Natural Porous Media. *SPE Res Eng* **5** (3): 361–368. SPE-18283-PA. https://doi.org/10.2118/18283-PA.

Computer Modelling Group. 2018. STARS Version 2018 User's Guide. Calgary, Alberta, Canada: Computer Modelling Group.

Das, S. K. 1998. Vapex: An Efficient Process for the Recovery of Heavy Oil and Bitumen. *SPE J.* **3** (3): 232–237. SPE-50941-PA. https://doi.org/10.2118/50941-PA.

Deng, X., Huang, H., Zhao, L. et al. 2010. Simulating the ES-SAGD Process with Solvent Mixture in Athabasca Reservoirs. *J Can Pet Technol* **49** (1): 38–46. SPE-132488-PA. https://doi.org/10.2118/132488-PA.

Dong, L. 2012. Effect of Vapour-Liquid Phase Behaviour of Steam—Light Hydrocarbon Systems on Steam Assisted Gravity Drainage Process for Bitumen Recovery. *Fuel* **95:** 159–168. https://doi.org/10.1016/j.fuel.2011.10.044.

Haugen, Å., Fernø, M. A., Mason, G. et al. 2015. The Effect of Viscosity on Relative Permeabilities Derived from Spontaneous Imbibition Tests. *Transp Porous Media* **106** (2): 383–404. https://doi.org/10.1007/s11242-014-0406-4.

Hosseininejad Mohebati, M., Maini, B. B., and Harding, T. G. 2012. Experimental Investigation of the Effect of Hexane on SAGD Performance at Different Operating Pressures. Paper presented at the SPE Heavy Oil Conference Canada, Calgary, Alberta, Canada, 12–14 June. SPE-158498-MS. https://doi.org/10.2118/158498-MS.

Ivory, J. J., Zheng, R., Nasr, T. N. et al. 2008. Investigation of Low Pressure ES-SAGD. Presented at the International Thermal Operations and Heavy Oil Symposium, Calgary, Alberta, Canada, 20–23 October. SP E-117759-MS. https://doi.org/10.2118/117759-MS.

Jha, R. K., Kumar, M., Benson, I. et al. 2013. New Insights into Steam/Solvent-Coinjection-Process Mechanism. *SPE J.* **18** (5): 867–877. SPE-159277-PA. https://doi.org/10.2118/159277-PA.

Kalaydjian, F. 1990. Origin and Quantification of Coupling between Relative Permeabilities for Two-Phase Flows in Porous Media. *Transp Porous Media* **5** (3): 215–229. https://doi.org/10.1007/BF00140013.

Khalifi, M., Zirrahi, M., Hassanzadeh, H. et al. 2020. Concentration-Dependent Molecular Diffusion Coefficient of Dimethyl Ether in Bitumen. *Fuel* **274:** 117809. https://doi.org/10.1016/j.fuel.2020.117809.

Keshavarz, M., Okuno, R., and Babadagli, T. 2014. Efficient Oil Displacement near the Chamber Edge in ES-SAGD. *J Pet Sci Eng* **118:** 99–113. https://doi.org/10.1016/j.petrol.2014.04.007.

Keshavarz, M., Okuno, R., and Babadagli, T. 2015. Optimal Application Conditions for Steam/Solvent Coinjection. *SPE Res Eval & Eng* **18** (1): 20–38. SPE-165471-PA. https://doi.org/10.2118/165471-PA.

Khaledi, R. R., Beckman, M. S., Pustanyk, K. et al. 2012. Physical Modeling of Solvent-Assisted SAGD. Paper presented at the SPE Heavy Oil Conference Canada, Calgary, Alberta, Canada, 12–14 June. SPE-150676-MS. https://doi.org/10.2118/150676-MS.

Khaledi, R. R., Boone, T. J., Motahhari, H. R. et al. 2015. Optimized Solvent for Solvent Assisted-Steam Assisted Gravity Drainage (SA-SAGD) Recovery Process. Paper presented at the SPE Canada Heavy Oil Technical Conference, Calgary, Alberta, Canada, 9–11 June. SPE-174429-MS. https://doi.org/10.2118/174429-MS.
Mendoza de la Cruz, J. L., Arguelles-Vivas, F. J., Matias-Perez, V. et al. 2009. Asphaltene-Induced Precipitation and Deposition during Pressure Depletion on a Porous Medium: An Experimental Investigation and Modeling Approach. *Energy Fuels* **23** (11): 5611–5625. https://doi.org/10.1021/ef9006142.
Mohammadi, M., Haddadnia, A., Zirrahi, M. et al. 2020. Interfacial Tension of n-Pentane/Bitumen and n-Heptane/Bitumen Mixtures at $T=$ 298.15–413.15 K and $P=$ 3.45 MPa. *J Chem Eng Data* **65** (4): 1787–1794. https://doi.org/10.1021/acs.jced.9b01073.
Mukhametshina, A., Kar, T., and Hascakir, B. 2016. Asphaltene Precipitation during Bitumen Extraction with Expanding-Solvent Steam-Assisted Gravity Drainage: Effects on Pore-Scale Displacement. *SPE J*. **21** (2): 380–392. SPE-170013-PA. https://doi.org/10.2118/170013-PA.
Nasr, T. N., Beaulieu, G., Golbeck, H. et al. 2003. Novel Expanding Solvent-SAGD Process "ES-SAGD." *J Can Pet Technol* **42** (1): 13–16. PETSOC-03-01-TN. https://doi.org/10.2118/03-01-TN.
Okuno, R. 2018. Coinjection of Dimethyl Ether and Steam for Bitumen and Heavy Oil Recovery. US Patent No. 10,125,591.
Ovalles, C. 2019. *Subsurface Upgrading of Heavy Crude Oils and Bitumen*. Boca Raton, Florida, USA: CRC Press.
Prats, M. 1982. *Thermal Recovery*, Vol. 7. Richardson, Texas, USA: Monograph Series, Society of Petroleum Engineers.
Robinson, D. B. and Peng, D. Y. 1978. The Characterization of the Heptanes and Heavier Fractions for the GPA Peng-Robinson Programs. Research Report RR-28, Gas Processors Association, Tulsa, Oklahoma, USA.
Sheng, K., Argüelles-Vivas, F. J., Baek, K. et al. 2020a. An Experimental Study of Emulsion Flow in Alkaline/Solvent Coinjection with Steam for Heavy-Oil/Bitumen Recovery. *SPE Res Eval & Eng* **23** (2): 402–413. SPE-190224-PA. https://doi.org/10.2118/190224-PA.
Sheng, K., Okuno, R., Imran, M. et al. 2020b. An Experimental Study of Steam-Assisted Gravity Drainage. *SPE J*. 1–20. SPE-200867-PA. https://doi.org/10.2118/200867-PA.
Sheng, K., Okuno, R., and Wang, M. 2018. Dimethyl Ether as an Additive to Steam for Improved Steam-Assisted Gravity Drainage. *SPE J*. **23** (4): 1201–1222. SPE-184983-PA. https://doi.org/10.2118/184983-PA.
Venkatramani, A. and Okuno, R. 2017. Compositional Mechanisms in SAGD and ES-SAGD with Consideration of Water Solubility in Oil. *SPE Res Eval & Eng* **20** (3): 681–697. SPE-180737-PA. https://doi.org/10.2118/180737-PA.
Venkatramani, A. and Okuno, R. 2018. Mechanistic Simulation Study of Expanding-Solvent Steam-Assisted Gravity Drainage under Reservoir Heterogeneity. *J Pet Sci Eng* **169:** 146–156. https://doi.org/10.1016/j.petrol.2018.04.074.
Zirahi, A., Yamchi, H. S., Haddadnia, A. et al. 2020. 2-D Physical Model Experimental Study of Ethyl Acetate and Steam Co-Injection for In-Situ Bitumen Recovery. *Fuel* **265:** 116943. https://doi.org/10.1016/j.fuel.2019.116943.

Appendix A—Fluid Models for Numerical Simulation

In this appendix, we provide the data and modeling methods for the fluid models used for the history matching in STARS. The data and models in this appendix include the EOS model, viscosity, and density models.

The condensate was modeled by assuming four normal alkane components: C_1, C_4, C_8, and C_{12}. The bitumen was characterized with the PR EOS with B1 (distillable fraction) and B2 (nondistillable fraction) by matching bubblepoints. The bubblepoints were measured with constant mass expansion for the condensate and four condensate/bitumen mixtures as given in **Table A-1.** The resulting EOS model is given in **Table A-2.**

Mixture/Temperature	50°C	100°C	150°C	200°C
40.1-mol% solvent	Not measured	553	724	993
60.9-mol% solvent	Not measured	629	820	1138
90.0-mol% solvent	Not measured	644	931	1271
94.4-mol% solvent	Not measured	653	995	1322
100-mol% solvent	643	868	1,074	1450

Table A-1—Bubblepoint pressures (kPa) measured by constant expansion experiment for condensate/bitumen mixtures.

The densities of the condensate/bitumen mixtures were calculated from the constant mass expansion experiments **(Table A-3).** STARS models oil-phase densities assuming the following:

$$1/\rho_L = \sum_{i=1}^{Nc} x_{iL}/\rho_{iL}, \quad \text{(A-1)}$$

where ρ_L is the molar density of oil phase, x_{iL} is the mole fraction of component i in the oil phase, and N_C is the number of components. ρ_{iL} is the molar density of each component modeled as

$$\rho_{iL} = \rho_{i\mathrm{ref}} \exp\left[-\alpha_1(T - T_{\mathrm{ref}}) - \frac{1}{2}\alpha_2\left(T^2 - T_{\mathrm{ref}}{}^2\right) + \alpha_3(P - P_{\mathrm{ref}}) + \alpha_4(P - P_{\mathrm{ref}})(T - T_{\mathrm{ref}})\right], \quad \text{(A-2)}$$

where P_{ref} and T_{ref} are the reference pressure and temperature, 101.3 kPa and 15.56°C. $\rho_{i\mathrm{ref}}$ is the molar density of component i at these conditions. α and $\rho_{i\mathrm{ref}}$ were obtained by matching the density data in Table A-3. **Table A-4** shows the calibrated density models for STARS.

Table A-5 shows the viscosities measured for three condensate/bitumen mixtures. Together with the bitumen viscosity data from Sheng et al. (2020b), the oil viscosities are modeled in STARS using the weighted log-linear mixing of pure components:

$$\ln\mu_L = \sum_{i=1}^{Nc} q_i x_i \ln\mu_i = \sum_{i=1}^{Nc} f_i \ln\mu_i, \quad \text{(A-3)}$$

where μ_L is the oil phase viscosity, and μ_i, q_i, and x_i are the viscosity, scaling factor, and molar fraction of component i, respectively. To satisfy the material balance, the summation of $q_i x_i$ for all the components should be equal to unity. The heaviest component, B2, was set as the key component, and therefore the f_{B2} table was given to STARS. The weighting factors for all the non-key components were set to be identical with one another. **Table A-6 and Fig. A-1** show the resulting viscosity inputs for STARS.

(a) Concentrations, critical properties, acentric factors, and molecular weights.

Component	Mol%	Molecular Weight (g/mol)	T_c (°C)	P_c (kPa)	Acentric Factor
		Condensate			
C_1	2.3	16.0	–82.55	4600	0.0080
n-C_4	9.8	58.1	152.05	3800	0.1930
n-C_8	81.5	114.2	295.65	2482	0.3940
n-C_{12}	6.4	170.3	385.15	1824	0.5620
		Dead Bitumen			
B1	49.5	283.0	526.35	2000	0.3996
B2	50.5	831.1	976.62	1314	0.8712

(b) Binary interaction parameters for two-pseudocomponent bitumen model.

	C_1	*n*-C_4	*n*-C_8	*n*-C_{12}	B1	B2
C_1	0					
n-C_4	0.0420	0				
n-C_8	0.0500	0.0337	0			
n-C_{12}	0.0536	0.0482	0	0		
B1	0.0599	0.0625	0	0	0	
B2	0.0925	0.0795	0	0	0	0

Table A-2—EOS model for STARS. The PR EOS model was calibrated with experimental data. Water dissolution in oil is not considered.

	100°C		150°C		200°C	
	Pressure (kPa)	Density (kg/m^3)	Pressure (kPa)	Density (kg/m^3)	Pressure (kPa)	Density (kg/m^3)
40.1-mol% solvent	968	900.2	1092	870.9	1444	841.4
	750	899.7	919	869.7	1305	840.7
	625	899.4	804	868.9	1163	840.3
	558	899.2	786	868.9	1035	839.8
60.9-mol% solvent	1360	857.4	1961	826.8	1812	793.8
	1015	856.8	1201	825.1	1320	792.5
	859	856.4	1064	824.7	1185	792.0
	713	856.1	905	824.2	1148	791.2
90.0-mol% solvent	1223	724.3	1351	685.9	2078	644.9
	1031	723.9	1203	685.5	1739	644.0
	889	723.6	1136	685.4	1461	643.1
	741	723.3	1030	685.2	1300	642.3
94.4-mol% solvent	1379	689.8	1625	649.4	1940	599.7
	1052	689.0	1451	648.9	1704	599.6
	886	688.7	1293	648.4	1564	599.1
	719	688.3	1062	647.5	1391	598.4

Table A-3—Measured densities of four condensate/bitumen mixtures by constant-mass expansion experiment.

	C_1	*n*-C_4	*n*-C_8	*n*-C_{12}	B1	B2
ρ_{ref} (kg/m^3)	320.21	583.37	705.41	752.73	836.00	1092.08
α_1 (°C^{-1})	1.32×10^{-3}	5.65×10^{-5}	5.95×10^{-5}	5.04×10^{-5}	1.50×10^{-4}	6.34×10^{-4}
α_2 (°C^{-2})	5.77×10^{-6}	7.93×10^{-6}	3.63×10^{-6}	2.87×10^{-6}	1.12×10^{-6}	7.48×10^{-8}
α_3 (kPa^{-1})	5.13×10^{-5}	4.82×10^{-6}	3.44×10^{-6}	1.61×10^{-6}	9.47×10^{-7}	6.71×10^{-8}
α_4 (kPa^{-1}°C^{-1})	4.05×10^{-8}	1.20×10^{-8}	4.56×10^{-9}	9.50×10^{-9}	4.16×10^{-9}	2.17×10^{-10}

Table A-4—Density model for STARS.

	Pressure (kPa)	72°C	100°C	130°C	150°C	170°C
40.1-mol% solvent mixture	2000	44.35	17.66	7.52	5.05	3.54
	3000	44.99	17.94	7.61	5.13	3.59
	4000	45.91	18.25	7.73	5.18	3.62
	6000	47.53	19.12	7.95	5.31	3.70
	8000	49.12	19.92	8.12	–	–
	10 000	50.49	20.88	8.26	–	–
60.9-mol% solvent mixture	2000	16.41	7.13	3.82	2.63	1.91
	3000	16.81	7.22	3.89	2.68	1.93
	4000	16.98	7.35	3.93	2.72	1.95
	6000	17.46	7.48	3.99	2.79	2.01
	8000	17.97	7.73	4.06	–	–
	10 000	18.36	8.02	4.15	–	–
90.0-mol% solvent mixture	2000	0.829	0.541	0.357	0.291	0.221
	3000	0.830	0.542	0.358	0.292	0.222
	4000	0.831	0.543	0.359	0.293	0.222
	6000	0.833	0.544	0.359	0.293	0.223
	8000	0.834	0.545	0.360	–	–
	10 000	0.836	0.546	0.361	–	–

Table A-5—Measured viscosities for three condensate/bitumen mixtures.

Mole Fraction	f_{B2}
0	0.0000
0.1	0.1679
0.2	0.2508
0.3	0.3136
0.4	0.4020
0.5	0.5002
0.6	0.6000
0.7	0.7000
0.8	0.8000
0.9	0.9000
1	1.0000

Table A-6—Scaling factor f_{B2}: composition table for the viscosity model for STARS.

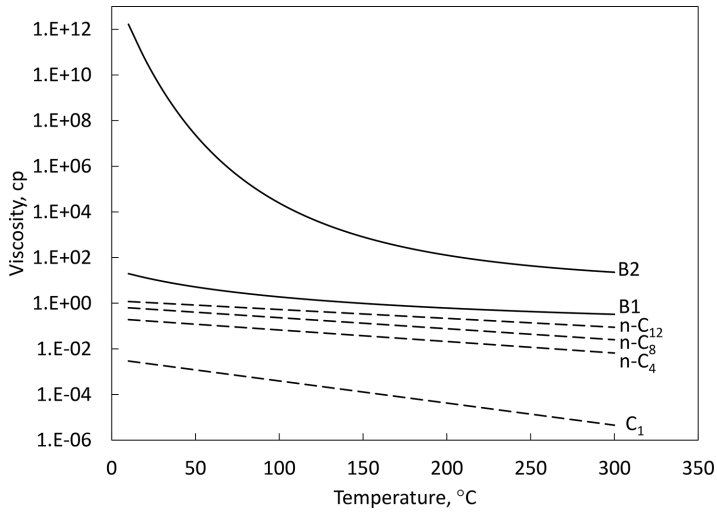

Figure A-1—Apparent viscosity model for each component used for the simulation with STARS.